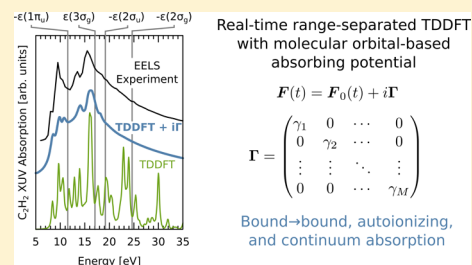


Near and Above Ionization Electronic Excitations with Non-Hermitian Real-Time Time-Dependent Density Functional Theory

Kenneth Lopata^{*,†} and Niranjana Govind^{*}

William R. Wiley Environmental Molecular Sciences Laboratory, Pacific Northwest National Laboratory, Richland, Washington 99352, United States

ABSTRACT: We present a real-time time-dependent density functional theory (RT-TDDFT) prescription for capturing near and post-ionization excitations based on non-Hermitian von Neumann density matrix propagation with atom-centered basis sets, tuned range-separated DFT, and a phenomenological imaginary molecular orbital-based absorbing potential to mimic coupling to the continuum. The computed extreme ultraviolet absorption spectra for acetylene (C_2H_2), water (H_2O), and Freon 12 (CF_2Cl_2) agree well with electron energy loss spectroscopy (EELS) data over the range of 0–50 eV. The absorbing potential removes spurious high-energy finite basis artifacts, yielding correct bound-to-bound transitions, metastable (autoionizing) resonance states, and consistent overall absorption shapes.



1. INTRODUCTION

Light-induced molecular excitations near and above the ionization threshold are of fundamental importance to a range of processes such as X-ray spectroscopy, the photo-damage of biomolecules, superexcited states, and autoionization. Moreover, the mechanisms of, and downstream chemical dynamics resulting from, these types of excitations are now accessible to cutting-edge ultrafast experiments;^{1–4} however, many issues remain. Metastable states are of particular interest, where electronic excitations to above the ionization limit persist for a finite lifetime before autoionizing. Broadly speaking, these autoionizing states can be broken into two classes:⁵ shape resonances, where the singly excited state of molecule A is above the energy of an electron-detached ($A^+ + e^-$) state; and Feshbach resonances, where the excited state is below its own continuum but above another ionization threshold.

Autoionizing states have attracted much theoretical attention with a wide range of both Hermitian and non-Hermitian approaches, of which we mention only a selection. Among Hermitian techniques, resonances have been studied using explicit time-dependent methods on small systems,^{6–9} dressed time-dependent density functional theory (TDDFT),¹⁰ and TDDFT with coupling to the continuum,¹¹ to name only a few. For non-Hermitian studies, most approaches involving either complex-scaling^{12,13} or complex-absorbing potentials.¹⁴ In the complex-scaling literature, recent efforts have ranged from time-dependent Schrödinger equation studies on one-dimensional (1D) systems,¹⁵ to quantum chemistry methods such as TDDFT,¹⁶ the random-phase approximation,¹⁷ equation-of-motion coupled cluster,¹⁸ and configuration interaction.¹³ Absorbing boundaries, which emulate the unbound wave function propagating out to infinity, are perhaps best known for their use in wavepacket calculations¹⁴ and molecular conductance simulations,^{19–21} and these have been applied to resonances using complex configuration interaction,²² and

complex density functional theory (DFT),²³ as well as planewave²⁴ and grid-based²⁵ real-time TDDFT studies.

Despite these advances, computing the spectroscopic response of resonance states remains a significant challenge, which has limited progress toward first-principles simulations of the dynamics initiating (and resulting from) autoionization processes. For dynamics simulations, TDDFT²⁶ has great promise, because of its long track record of successfully capturing a wide range of molecular excitations at modest computational cost.²⁷ Using TDDFT for these excitations, however, is problematic, because the states are highly diffuse (i.e., Rydberg) or even continuum-like (planewaves), which not only makes significant demands on atom-centered basis sets (e.g., Gaussians, Slater's, etc.) but also brings the validity of the DFT exchange-correlation functional into question. Moreover, since the picture of discrete eigenstates breaks down in the continuum, traditional frequency-domain TDDFT approaches such as Davidson solvers become problematic. In the TDDFT literature, these are often applied in a grid-based representation to describe the wave function distant from the atoms. However, atom-centered functions are often the preferred basis for molecular calculations for efficiency and implementation reasons, and also for processes involving core electrons (e.g., X-ray absorption^{28,29}) where grids and planewaves have difficulty describing the wave function near the nucleus. Finally, from a first-principles dynamics standpoint, a real-time TDDFT approach^{30–35} is a natural starting point.

Thus, as a first step toward first-principles ionization dynamics, in this paper, we present a prescription for reliably describing a wide range of below- and above-ionization spectral features in molecules using real-time TDDFT. The remainder of the paper takes the following form: in section 2, we outline

Received: July 1, 2013

the methodology; in section 3, we present simulated absorption spectra of a series of gas-phase molecules, and, finally, we summarize our findings in section 4.

2. METHODOLOGY

In a nutshell, we apply an imaginary potential in the molecular orbital space, which acts on virtual orbitals above the ionization level but not on the occupied or bound virtuals, which gives the unbound virtuals a finite lifetime before they autoionize. This approach is an alternative to traditional spatial absorbing boundaries, which mimic wave function propagation out of the finite simulation box. Since the imaginary potential makes the Fock matrix non-Hermitian, the norm of the wave function (or trace of the density matrix) is no longer conserved when the above-ionization virtuals are occupied. This is fundamentally different from simply applying a finite lifetime to the excited states, since, here, the charge is drained from the system rather than relaxed to the ground state. Also, since the potential is applied to the molecular orbitals themselves, the absorbing potentials have the added benefit of “filtering out” spurious virtual states arising from either the finite basis set or the inaccuracies of the DFT exchange-correlation functional without requiring a larger basis set. We use three ingredients in our approach: tuned range-separated DFT for an improved description of the high-lying states (section 2.1), an imaginary potential in MO space to mimic coupling to the continuum (section 2.2), and finally non-Hermitian time propagation of the density matrix (section 2.3).

2.1. Tuned Range-Separated DFT. High-energy excitations (e.g., Rydberg states) are known to be problematic for TDDFT, with the error largely arising from the improper asymptotic form of the exchange-correlation (XC) potential. Near- and above-ionization excitations, which involve very diffuse (even planewave-like) states, are even more challenging. This limitation can be remedied somewhat by using asymptotic corrections spliced onto the XC potential, as in LB94³⁶ and CS00.^{37,38} Since these are potential-only corrections and are not derived from an energy functional, the quality of their response properties can be suspect, since there is ambiguity in how one constructs the energy functional.³⁹ When used in traditional linear-response (frequency domain) TDDFT, their response is not included and their effect is only to shift the raw eigenvalues. Using these potentials in real-time TDDFT, however, implicitly includes their higher derivative response so care must be taken. Nevertheless, LB94 has been used successfully in conjunction with grid-based real-time studies of continuum excitations.²⁵

A more elegant approach, however, is to instead use range-separated functionals such as BNL, CAM-B3LYP, LC-PBE, etc., where the exchange term of the energy functional is decomposed into short-range and long-range parts (see the review by Baer et al.⁴⁰):

$$\frac{1}{r_{12}} = \frac{\alpha + \beta \operatorname{erf}(\mu r_{12})}{r_{12}} + \frac{1 - [\alpha + \beta \operatorname{erf}(\mu r_{12})]}{r_{12}} \quad (1)$$

with the short-range part being treated with DFT exchange and the long-range part with Hartree–Fock exchange. Here, α and β are dimensionless parameters that control the asymptotic amounts of DFT versus HF exchange: as $r_{12} \rightarrow 0$ you get an α fraction of HF and a $(1 - \alpha)$ fraction of DFT exchange, and as $r_{12} \rightarrow \infty$ you get $(\alpha + \beta)$ HF and $(1 - \alpha - \beta)$ DFT exchange. The attenuation parameter μ (dimensions of inverse length;

typically given in units of a_0^{-1}) determines how quickly the XC functional switches from DFT to HF exchange.

Range-separated functionals are especially powerful when α , β , and μ are tuned from “first principles” to minimize errors in certain physical quantities (e.g., the first ionization potential),^{40–42} which significantly improves their accuracy for charge-transfer or Rydberg excitations without input from experiment (see Perspective by Kronik et al.⁴³). For example, the LC-PBE functional goes from pure PBE exchange in the short-range to pure HF in the long-range, i.e., $\alpha = 0$, $\beta = 1$. The energy expression is then, schematically,

$$E_{\text{XC}}[\rho, \{\psi\}] = E_{\text{X}}^{\text{PBE,short}}[\rho] + E_{\text{X}}^{\text{HF,long}}[\{\psi\}] + E_{\text{C}}^{\text{PBE}}[\rho] \quad (2)$$

with the corresponding range-separation expression described by eq 1 reducing to

$$\frac{1}{r_{12}} = \frac{\operatorname{erf}(\mu r_{12})}{r_{12}} + \frac{1 - \operatorname{erf}(\mu r_{12})}{r_{12}} \quad (3)$$

The LC-PBE functional can then be tuned by varying the single parameter μ to ensure that the Koopmans’ ionization potential (IP) condition ($\text{IP} = -\epsilon_{\text{HOMO}}$) is satisfied, i.e., by minimizing the object function (for a neutral molecule):

$$J(\mu) = \left| \text{IP}_{\text{SCF}}(\mu) - \text{IP}_{\text{Koopmans}}(\mu) \right| \quad (4)$$

$$= |E_{\text{SCF}}^{\text{cation}}(\mu) - E_{\text{SCF}}^{\text{neutral}}(\mu) + \epsilon_{\text{HOMO}}^{\text{neutral}}| \quad (5)$$

where SCF denotes ground-state Kohn–Sham energies, and ϵ_{HOMO} is the HOMO eigenvalue. The resulting tuned functional, which is system-dependent, is denoted LC-PBE*. In general, multidimensional fitting with α , β , and μ , along with object functions more complicated than eq 5, can be used for other functionals,^{41,42} but here we exclusively use LC-PBE* tuned via the first IP. In practice, tuning brings the SCF and Koopmans’ IP to within 1% of each other, and the corresponding value to within a few percent of experimental values. Despite the obvious utility of this approach, it is worth noting that tuning range-separated hybrids can also introduce serious problems such as size inconsistency, which arises when distant molecular fragments have different tuning parameters than the aggregate system.⁴⁰

2.2. Absorbing Boundary Conditions in the Molecular Orbital Space. Next, we discuss the use of absorbing boundary conditions to emulate the continuum. The idea here is that, although DFT with atom-centered basis sets cannot describe excitations above the ionization limit, we can mimic the effect of an electron leaving the system with a nonphysical potential akin to an imaginary absorbing boundary condition (ABC). In grid-based DFT, an obvious approach is to apply an imaginary smoothly increasing potential at the edges of the simulation, which will remove charge that reaches this boundary region without nonphysical reflections. In an atom-centered basis set approach, however, this is problematic since the region of space far from a nucleus is poorly described, unless one resorts to a grid of “ghost” atoms, which has both efficiency and numerical convergence issues. A more effective approach is to apply an imaginary potential directly to the Fock matrix in the molecular orbital (MO)/orthogonal representation. This ABC can then be eigenvalue-dependent, with a smoothly increasing strength (decreasing lifetime) as a function of MO eigenvalue ensuring no nonphysical “reflections” in function space. We note that this extends Kohn–Sham DFT in

a spirit similar to the DFT+U method, where the phenomenological and orbital-dependent U parameter is used to correct an LDA or GGA approach in order to capture strong electronic correlations. The first step is construction of a diagonal damping matrix:

$$\Lambda = \begin{pmatrix} \gamma_1 & 0 & \cdots & 0 \\ 0 & \gamma_2 & \cdots & 0 \\ \vdots & \vdots & \ddots & \vdots \\ 0 & 0 & \cdots & \gamma_M \end{pmatrix} \quad (6)$$

where M is the number of molecular orbitals (MOs), and γ_i is the phenomenologically chosen damping parameter for the i th MO. In order to apply this potential to the Hamiltonian, this diagonal matrix is projected onto the instantaneous (time-dependent) MO eigenvectors:

$$\Gamma'(t) = C'(t)\Lambda C'^{\dagger}(t) \quad (7)$$

Note the ordering of the matrices, which corresponds to a “reverse” projection. Here, $C'(t)$ is the matrix with columns constructed from the eigenvectors of the time-dependent Fock matrix in the MO basis (note prime means MO basis; no prime means AO basis). In the limit of weak excitation (linear response), $\Gamma'(t)$ becomes time-independent and thus only needs to be constructed once, meaning the absorbing boundary procedure is essentially free computationally. Since, in this paper, we are primarily interested in spectroscopic data, this assumption is valid. Modeling strong-field response or ionization events, however, requires projection onto the time-dependent Fock matrix at every time step. $\Gamma'(t)$ can now be added directly to the time-dependent MO Fock matrix during propagation,

$$\mathbf{F}'(t) = \mathbf{F}'_0(t) + i\Gamma'(t) \quad (8)$$

or alternately converted to the atomic orbital (AO) basis and added after the Fock matrix construction:

$$\Gamma(t) = \mathbf{Y}\Gamma'(t)\mathbf{Y}^{\dagger} \quad (9)$$

where $\mathbf{Y} \equiv \mathbf{V}\mathbf{s}^{1/2}$ is the canonical orthogonalization transform matrix constructed from the eigenvalues (s) and eigenvectors (\mathbf{V}) of the overlap matrix (see ref 35 for details). This transform is time-independent if the basis set is invariant in time, e.g., if the nuclei are frozen.

Drawing inspiration from the exponential shape of continuum absorption, we pick an exponentially increasing damping acting on all MOs in the continuum:

$$\gamma_i = \begin{cases} 0 & \tilde{\varepsilon}_i \leq 0 \\ \gamma_0[\exp(\xi\tilde{\varepsilon}_i) - 1] & \tilde{\varepsilon}_i > 0 \end{cases} \quad (10)$$

where $\tilde{\varepsilon}_i = \varepsilon_i - \varepsilon_0$ is energy of the i th MO above the vacuum cutoff energy ε_0 (discussed next), ξ is a parameter dictating the “steepness” of the ABC (dimensions of inverse energy), and γ_0 (dimensions of energy) sets the energy scale. The corresponding lifetimes of each MO (before the electron is drained from the system) is

$$\tau_i = \frac{1}{2\gamma_i} \quad (11)$$

For example, if $\gamma_0 = 1.0\text{ Ha}$ and $\xi = 0.5\text{ Ha}^{-1}$, an MO lying 1 eV above the vacuum level (1 eV = 37 mHa) would have a lifetime

of 54 au = 1.3 fs, and thus will have a full width at half-maximum (fwhm) of ~1 eV in the absorption spectrum. In practice, the value of γ_i is clamped (e.g., 1000 Ha) to avoid numerical problems with large numbers; at this point, these states have effectively zero lifetime. One possible alternate prescription for the absorbing potential (eq 10) is to instead dictate the lifetime of each MO directly from its spatial extent, with a critical “diffusivity” above which each MO is unbound. With atom-centered basis sets, however, the high-lying (above-ionization) MOs are likely to have highly nonphysical shapes so this approach may be problematic.

Finally, it is important to note that one serious drawback of an absorbing potential of the form described by eq 10 is that the action of such a potential can potentially mimic damping arising from an indeterminate range of physical processes, both intramolecular as well as due to the environment, with no clear distinction between them. For the results in this paper, at least, this is not a critical problem because the experiments against which we make comparisons were performed under vacuum. Similarly, imaginary potentials of analogous form have been successfully applied to real-time CI ionization dynamics simulations in gas-phase LiCN and H₂.⁴⁴ However, generally, the validity of these types of phenomenological potentials is suspect for systems in more-complex environments.

In order to use eq 10, we must label the virtual MOs as either bound or in the continuum. A rough measure is sign of the electron affinity (EA) of each virtual orbital, with negative EAs corresponding to bound states and positive EAs corresponding to continuum states. This step is necessary since you cannot construct the absorbing potential from the TDDFT excitation energies directly; each TDDFT root is formed of a linear combination of MOs and thus there is no single matrix (MO-dependent potential) of the form described by eq 6.

Rather than use the raw virtual eigenvalues which are, generally, highly basis-set-dependent, we can instead approximate the EA of each virtual orbital from the first EA combined with TDDFT, which includes orbital relaxation effects without problematic SCF convergence issues (e.g., using forced orbital occupation ΔSCF):

$$\text{EA}_1 = E^{\text{anion}} - E^{\text{neutral}} \quad (12)$$

$$\text{EA}_k \simeq \text{EA}_1 + v_{k-1} \quad k = 2, 3, \dots \quad (13)$$

In essence, instead of using the virtual orbital energies, which approach the zeroth-order EAs in the full basis limit, we compensate somewhat for the nonphysical basis set dependence by using corrected EAs instead.

In eq 13, v_k is the k th TDDFT excitation of the anion calculated using linear-response (frequency domain) TDDFT. To determine the vacuum energy level ε_0 in eq 10, we interpolate the eigenvalues to the value such that EA equals zero. Since electron affinities can be highly basis dependent, large diffuse basis sets must be used to get a reliable labeling for the virtual states. In practice this typically results in the first few (~5) virtual MOs being bound. Of course, using a grid-based ABC avoids this somewhat arbitrary step completely, but is unsuitable for an atom-centered basis implementation, as discussed above.

Finally, since Γ is purely positive it is guaranteed to remove electrons from the system. This can be seen easily for a time-independent Fock matrix which has the exact solution:

$$|\psi_i(t)\rangle = \exp[i\mathbf{F}'t]|\psi_i(0)\rangle \quad (14)$$

$$= \exp[i\mathbf{F}'_0t - \mathbf{\Gamma}'t]|\psi_i(0)\rangle \quad (15)$$

Since the potential only acts on “unbound” virtual MOs, in the absence of an electric field perturbation, there are no dynamics and the charge is conserved. Moreover, a kick-type excitation spreads energy equally across all frequencies and thus very few electrons will be ionized from the system during propagation, which means the overall system charge is effectively constant, despite the non-Hermiticity of the Fock matrix. For concreteness, after each simulation in this paper, a total of less than $\sim 10^{-7}$ electrons were removed from the system. A resonant (e.g., continuous wave) excitation, on the other hand, would result in significant ionization. Conversely, a purely negative potential will, instead, add electrons into the specified MOs and could potentially be used to mimic electron flux into the system.

It is important to note that this approach is fundamentally different from energy-dependent broadening, e.g., post-processing via convolution with Lorentzians of energy-dependent widths. In the broadening approach, the oscillator strengths are preserved (e.g., the area under the curve), thus spurious excitations remain, albeit spread over a large frequency range. With the ABC approach, low-lying above-ionization excitations can have finite lifetimes (e.g., autoionizing resonance states) while far-above ionization excitations are removed completely. More importantly, the ABC approach removes the contributions of continuum “molecular orbitals” from multiconfiguration-like excitations, which is especially important for near-ionization excitations which often have significant contributions from both bound and unbound virtuals MOs. In this way, the MO ABC technique is similar to rotating the eigenvalues into the complex plane, as in complex scaling approaches,^{12,13,18} although, here, the lifetimes are phenomenological rather than computed.

2.3. Non-Hermitian Time Propagation. Inclusion of a complex-absorbing potential makes the effective Hamiltonian (Fock matrix) non-Hermitian, which requires some minor considerations when propagating the density matrix. See refs 30–35 for discussions of Hermitian real-time TDDFT. We first derive the non-Hermitian analogue of the von Neumann equation for the time derivative of the density matrix in the MO basis (prime notation). The time-dependent (TD) density matrix in terms of TD MOs is

$$\mathbf{P}'(t) = \sum_i p_i |\psi_i(t)\rangle \langle \psi_i(t)| \quad (16)$$

where p_i are the time-independent coefficients. Thus, the time derivative is (dot notation)

$$\dot{\mathbf{P}}'(t) = \sum_i p_i [|\dot{\psi}_i(t)\rangle \langle \psi_i(t)| + |\psi_i(t)\rangle \langle \dot{\psi}_i(t)|] \quad (17)$$

The TD Schrödinger equation and its Hermitian conjugate are given as

$$|\dot{\psi}_i(t)\rangle = -i\mathbf{F}'(t)|\psi_i(t)\rangle \quad (18)$$

$$\langle \dot{\psi}_i(t)| = i\langle \psi_i(t)|\mathbf{F}'(t)^\dagger \quad (19)$$

Thus, eq 17 becomes

$$\dot{\mathbf{P}}'(t + \Delta t) = \sum_i p_i [-i\mathbf{F}'(t)|\psi_i(t)\rangle \langle \psi_i(t)| + i|\psi_i(t)\rangle \langle \psi_i(t)|\mathbf{F}'(t)^\dagger] \quad (20)$$

$$= -i[\mathbf{F}'(t)\mathbf{P}'(t) - \mathbf{P}'(t)\mathbf{F}'(t)^\dagger] \quad (21)$$

which is akin to the von Neumann equation only with a crucial additional Hermitian conjugation. Equation 21 can be integrated in any number of ways but care must be taken that Hermiticity of \mathbf{F}' is not assumed. The exact solution to eq 21 takes the form

$$\mathbf{P}'(t + \Delta t) = \mathbf{U}(t + \Delta t, t)\mathbf{P}'(t)\mathbf{U}^\dagger(t + \Delta t, t) \quad (22)$$

where $\mathbf{U}(t + \Delta t, t)$ is now a nonunitary propagator. A second-order Magnus (exponential midpoint) scheme approximates this as

$$\mathbf{U}(t + \Delta t, t) \simeq e^{-i\mathbf{F}'(t+\Delta t/2)\Delta t} \quad (23)$$

(see ref 45). Here, the future-time Fock matrix $\mathbf{F}'(t + \Delta t/2)$ is first extrapolated from the previous two TD Fock matrices, then the density matrix propagated forward using eq 22, then finally the Fock matrix is recomputed using this updated density matrix. This self-consistent extrapolation–correction procedure is repeated each time step until convergence. Equation 23 can be constructed via power series exponentiation, for example, followed by taking the Hermitian conjugate to build eq 22, but other approaches that assume $\mathbf{H}'^\dagger = \mathbf{H}'$, such as Baker–Campbell–Hausdorff exponentiation, are not suitable. Alternately, explicit integration schemes (such as Runge–Kutta) can be used to integrate eq 21 directly, although they are typically inferior in stability and computational efficiency.

3. RESULTS

Next, we present the computed extreme ultraviolet (UV) absorption spectra of a few simple molecules. Schematically, the calculations were performed as follows:

- (1) Optimize geometry in the gas-phase: aug-cc-pVTZ/PBE0
- (2) Tune μ in LC-PBE via ionization potential using eq 5: aug-cc-pVTZ
- (3) Determine vacuum level using eq 13: d-aug-cc-pVQZ/LC-PBE*
- (4) Build time-independent imaginary absorbing potential using eq 10
- (5) Real-time TDDFT delta-function kick simulations: d-aug-cc-pVQZ/LC-PBE*

All simulations were performed using a development version of NWChem,^{46,47} and all basis sets were taken from the EMSL Basis Set Exchange.^{48–50} To construct the nonunitary propagator (eq 23) a second-order Magnus (exponential midpoint) scheme was used with self-consistent interpolation. Matrix exponentiation was carried out with a contractive power series (see refs 35 and 51 for details). No symmetry was assumed, so each absorption spectrum is the result of three simulations (x , y , z). The delta function kick strengths were chosen to be $\kappa = 10^{-4}$ au = 50 mV/nm. For all simulations, the time step was taken to be $\Delta t = 0.2$ au = 0.005 fs = 5 as and the total simulation time was $\Delta t = 500.0$ au = 12 fs. To accelerate convergence, before taking the Fourier transform the time-dependent dipole moments were damped with a decaying exponential with time constant $\tau = 108.9$ au = 2.6 fs, which

corresponds to uniformly Lorentzian broadened spectra with $\text{fwhm} = 0.5$ eV. Finally, since real-time TDDFT does not yield information about the orbitals involved in an excitation, traditional linear-response TDDFT^{52–54} was used to analyze the excitations in the absence of an absorbing boundary. For each of these calculations it was also explicitly checked that the Hermitian real-time and linear-response spectra are identical. All experimental data were taken from Brion's database of electron energy loss (EELS) dipole (e,e) spectra.⁵⁵

3.1. Acetylene Extreme Ultraviolet Absorption. First, we discuss the extreme ultraviolet (XUV) absorption of acetylene (C_2H_2), which has been well-studied experimentally^{56,57} and theoretically,^{11,17,58} with special attention paid to its autoionizing resonance states. For reference, the ground-state configuration (including the four lowest virtuals) is given by

$$(1\sigma_g)^2(1\sigma_u)^2(2\sigma_g)^2(2\sigma_u)^2(3\sigma_g)^2(1\pi_u)^4(1\pi_g)^0(3\sigma_u)^0(4\sigma_g)^0(4\sigma_u)^0 \quad (24)$$

The tuned aug-cc-pVTZ/LC-PBE* attenuation parameter was found to be $\mu = 0.415$ a_0^{-1} (see Table 1) with the resulting d-

Table 1. LC-PBE* Tuned Attenuation Parameters (μ) and the Corresponding Koopmans' ($-\epsilon_{\text{HOMO}}$) and ΔSCF ($E^{\text{anion}} - E^{\text{neutral}}$) Ionization Potentials (IPs), Compared with the Experimental Values^a

molecule	μ [a_0^{-1}]	$-\epsilon_{\text{HOMO}}$ [eV]	ΔSCF IP [eV]	expt IP [eV]
C_2H_2	0.415	11.52	11.52	11.40 ^b
H_2O	0.516	12.91	12.92	12.62 ^c
CF_2Cl_2	0.412	12.49	12.49	12.26 ^d

^aTuning was performed to minimize the error between the Koopmans' and ΔSCF IPs (see eq 5) using the aug-cc-pVTZ basis set. ^bData taken from ref 61. ^cData taken from ref 62. ^dData taken from ref 59.

Table 2. Computed (d-aug-cc-pVQZ/LC-PBE*) Koopmans' ($-\epsilon$) and Experimental Ionization Potentials for Acetylene (C_2H_2)

molecular orbital, MO	Ionization Potential (eV)	
	Koopmans, $-\epsilon$	experiment ^a
$1\pi_u$	11.52	11.40
$3\sigma_g$	17.07	16.36
$2\sigma_u$	19.18	18.69
$2\sigma_g$	24.64	23.50

^aData taken from ref 61.

aug-cc-pVQZ ionization potentials shown in Table 2. Note that the first IP is effectively independent of basis set. Tuning results in excellent agreement with the experimental values of the first four IPs (absolute errors ranging from 1% to 4%). The cutoff eigenvalue for the MO absorbing boundary conditions (ABC) was computed via a TDDFT electron affinity calculation to be $\epsilon_0 = 0.0284$ Ha = 0.77 eV (see eq 13) and the exponential constant was chosen to be $\xi = 0.5$ Ha⁻¹; the dependence of the spectrum on ξ will be discussed later.

Figure 1 shows the computed (RT-LC-PBE*/d-aug-cc-pVQZ) spectra with and without the imaginary potential, the corresponding DFT Koopmans' ionization potentials, and the experimental EELS spectrum.⁵⁷ We now discuss these spectra starting from the low-energy features and moving up. First, in

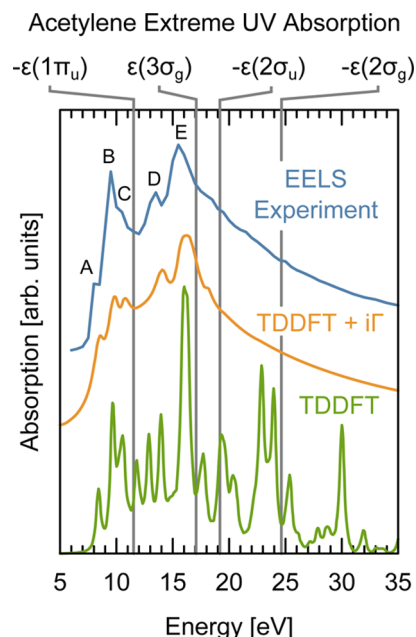


Figure 1. Real-time d-aug-cc-pVQZ/TD-LC-PBE* computed gas-phase extreme UV absorption spectrum of gas-phase acetylene (C_2H_2) with (orange) and without (green; scaled by 0.5) an imaginary absorbing potential ($i\Gamma$), along with the DFT Koopmans' ionization potentials (gray). The absorbing boundary exponential constant was taken to be $\xi = 0.5$ Ha⁻¹. The three lowest excitations (A, B, C), which correspond to excitations from the $1\pi_u$ molecular orbital (MO) to bound virtual MOs, are equally well-described by TDDFT with and without an absorbing potential, whereas an absorbing potential is required to properly describe the above-ionization region containing the two autoionizing resonance states (D, E). Electron energy loss spectroscopy (EELS) experimental spectrum (blue) taken from ref 57.

the experimental spectrum, there are three distinct low-energy excitations (peaks A, B, and C) below the first IP ($1\pi_u$). Since they are below ionization, these peaks are well-described by TDDFT both with and without an absorbing boundary (ABC), although the TDDFT+ $i\Gamma$ is broadened somewhat (in addition to the Lorentzian convolution). From linear-response TDDFT analysis, these peaks can be labeled as excitations from the $1\pi_u$ (HOMO, HOMO-1) orbital to bound virtuals.

Moving past the first ionization potential (DFT Koopmans': 11.40 eV), there are two broad experimental excitations at 13.3 eV (peak D) and 15.3 eV (peak E), which are traditionally attributed to autoionizing resonance states. These features, which can be challenging to capture,¹¹ are present in the TDDFT spectrum, because of the use of a tuned range-separated functional and large diffuse basis set. Although the resonance states are present in the spectrum, there are also other artifacts, specifically spurious excitations at ~ 10.5 eV and ~ 12.0 eV arising primarily from $1\pi_u \rightarrow$ high virtuals. The TDDFT+ $i\Gamma$, on the other hand, does not exhibit these artificial excitations and instead shows a smooth background absorption reminiscent of the experimental absorption shape. Moreover, the resonance excitations are significantly broadened beyond the Lorentzian convolution, which is a result of their finite lifetime, with widths/lifetimes qualitatively consistent with the experimental peaks. Looking at their linear-response character, peak E (experiment 15.3 eV, TDDFT 16.0 eV) roughly corresponds to excitations from the $2\sigma_u$, which is consistent with the assignment of this peak as a $2\sigma_u \rightarrow 1\pi_g$ intravalence autoionizing state.¹⁷ We calculate that peak D (experiment 13.3

eV, TDDFT 13.9 eV), which has been the source of some controversy, arises from excitations from $3\sigma_g$ and $1\pi_u$. Finally, past the second IP (DFT 16.36 eV) both the experimental and TDDFT+ $i\Gamma$ spectra show effectively featureless continuum falloff, whereas the TDDFT spectrum is dominated by artificial excitations resulting from the finite basis.

Since the absorbing boundary exponential constant ξ is phenomenological, we next explore the dependence of the spectrum on its value. Figure 2 shows the same TDDFT+ $i\Gamma$

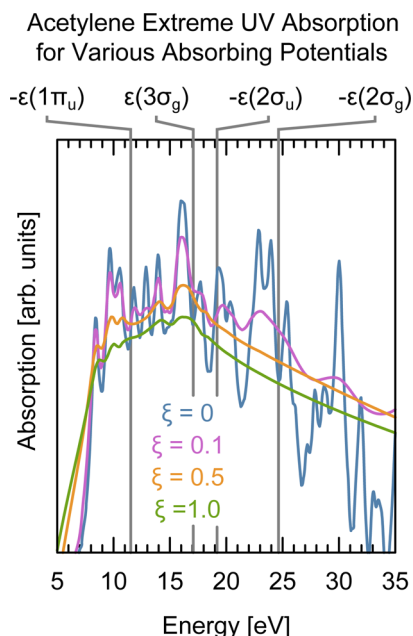


Figure 2. Extreme UV absorption spectrum (logarithmic scale) of acetylene (C_2H_2) computed using d-aug-cc-pVQZ/RT-TD-LC-PBE* with absorbing potentials of various strength (exponential constant, ξ ; units, Ha^{-1}). Increasing the potential strength increasingly removes spurious excitations to unbound molecular orbitals and broadens the metastable states (i.e., shorter lifetime). After a sufficiently large value (0.5 Ha^{-1}), the qualitative features are insensitive to the choice of ξ .

acetylene absorption spectrum (logarithmic scale) with ξ values: 0, 0.1 Ha^{-1} , 0.5 Ha^{-1} , and 1.0 Ha^{-1} . Adding a weak Γ ($\xi = 0.1 \text{ Ha}^{-1}$) reduces the overall absorption slightly and significantly reduces the two nonphysical peaks just past the first IP, as well as those above the higher IPs. Qualitatively, however, the artificial excitation remain as the ABC is insufficient to fully remove these states. Using an ABC parameter of $\xi = 0.5 \text{ Ha}^{-1}$ further reduces the absorption and also almost completely removes the spurious peaks, resulting in an exponential continuum falloff. Increasing to $\xi = 1.0 \text{ Ha}^{-1}$ reduces the absorption even more but the gross features are unchanged, albeit broadened somewhat (i.e., shorter lifetimes). There is also a minor shift in the lowest valence peak with increased ξ , likely due to the ABC removing contribution of molecular orbitals involved in this transition. Based on these results, we use $\xi = 0.5 \text{ Ha}^{-1}$ for all calculations.

3.2. Water Extreme Ultraviolet Absorption. Next, we study the extreme UV response of gas-phase water. The aug-cc-pVTZ/LC-PBE* attenuation was tuned via the first ionization potential to $\mu = 0.516a_0^{-1}$ (see Table 1) with the resulting IP within 2% of experiment. The cutoff eigenvalue for the absorbing potential was chosen to be $0.0477 \text{ Ha} = 13 \text{ eV}$ from a LR-TDDFT electron affinity calculation (eq 13) and the

ABC strength was taken to be $\xi = 0.5 \text{ Ha}^{-1}$. Figure 3 shows the d-aug-cc-pVQZ/RT-LC-PBE* computed and experimental

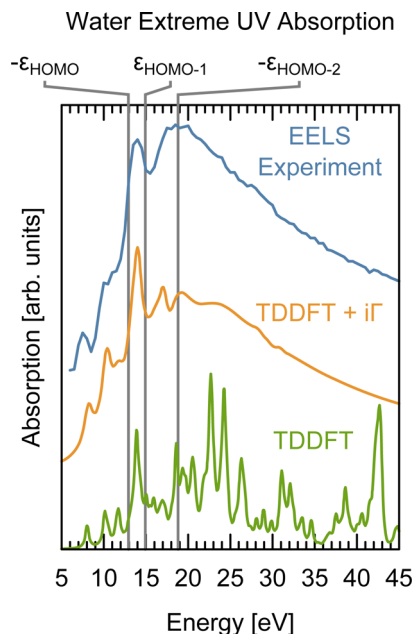


Figure 3. Real-time d-aug-cc-pVQZ/TD-LC-PBE* extreme UV absorption computed with an absorbing potential (orange; $\xi = 0.5 \text{ Ha}^{-1}$) and in the conventional manner (green; scaled by 0.5), compared with the experimental electron energy loss spectrum (taken from ref 63). The preionization (bound) features are relatively insensitive to the absorbing boundary, as is the strong resonance at $\sim 14 \text{ eV}$, whereas the post-ionization features arising from coupling to the continuum are only described correctly with TDDFT+ $i\Gamma$.

EELS absorption spectra. The first three excitations $\text{HOMO} \rightarrow \{\text{LUMO}, \text{LUMO}-1, \text{LUMO}-2\}$, which are below ionization, are adequately described without an absorbing potential. The TDDFT+ $i\Gamma$ spectrum exhibits a decreased third peak, most likely due to the absorbing potential incorrectly acting on these virtual states (i.e., poor choice of ϵ_0 and/or ξ). The strong resonance at $\sim 14 \text{ eV}$ (primarily $\text{HOMO}-2 \rightarrow \text{LUMO}, \text{LUMO}+4$) is properly captured with both methods, though broadened significantly in the TDDFT+ $i\Gamma$ spectrum due to the finite lifetime. Post-third ionization ($-\epsilon_{\text{HOMO}-2}$), the experimental data are dominated by the continuum absorption falloff, whose overall shape is captured by the TDDFT+ $i\Gamma$ spectrum, albeit with some additional features not present in experiment likely due to insufficient absorbing strength for these virtual states. In this region, the pure TDDFT spectrum is completely dominated by nonphysical peaks.

3.3. Freon 12 Extreme Ultraviolet Absorption. Finally, we present the extreme UV spectrum of Freon 12 (CF_2Cl_2), a well-known ozone-depleting chlorofluorocarbon (CFC) refrigerant that undergoes UV photodissociation in the stratosphere,



where the resulting $\text{Cl}\cdot$ radical catalyzes the conversion of O_3 to O_2 . The LC-PBE* parameter was IP tuned to $\mu = 0.412a_0^{-1}$, yielding an IP of 12.49 eV versus the experimental value of 12.26 eV .⁵⁹ The absorbing boundary cutoff (eq 10) was computed to be $0.0385 \text{ Ha} = 1.0 \text{ eV}$ and the strength chosen to be $\xi = 0.5 \text{ Ha}^{-1}$. Figure 4 shows the EELS⁶⁰ and d-aug-cc-pVQZ/RT-LC-PBE* spectra. Here, there is no simple

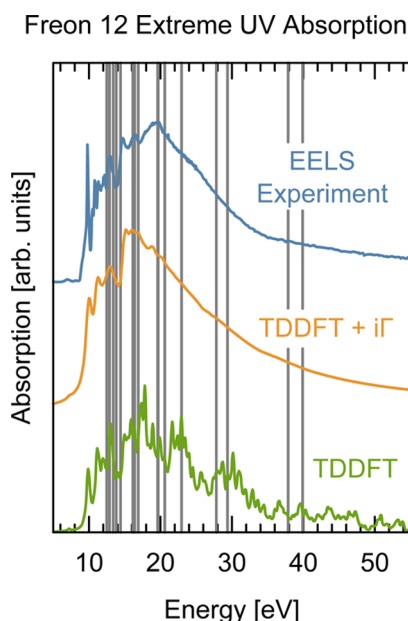


Figure 4. Computed (d-aug-cc-pVQZ/RT-LC-PBE*) extreme UV absorption spectrum of Freon 12 (CF_2Cl_2) with (orange) and without (green; scaled by 0.5) an absorbing potential. The outer and inner valence DFT Koopman's ionization potentials are shown for reference (gray vertical lines). The EELS experimental spectrum was taken from ref 60.

Koopman's ionization picture but rather a band-like ionization edge at ~ 13 eV. Below this threshold, there is a distinct low-energy absorption at ~ 7 eV, which corresponds to an excitation from the HOMO ($\text{Cl } p$ orbitals). Following that, there is a sharp absorption at ~ 10 eV (excitation from HOMO-4; $\text{Cl}+\text{F } p$), and a cluster of features at ~ 11 eV (HOMO, HOMO-1). The ionization features at ~ 13 eV and ~ 16 eV are captured by both methods and somewhat broadened by the absorbing potential, but features around the third ionization "band" (~ 20 eV) are inconsistent with the experimental data, likely due to overdamping by the absorbing potential (note the small absorption at ~ 19 eV). It is also interesting to note that the pure TDDFT spectrum roughly reflects the line shape of the TDDFT+ $i\Gamma$ which is likely a consequence of the larger spatial extent of the basis set on this molecule versus the two smaller molecules studied. Regardless, the TDDFT+ $i\Gamma$ method affords a significantly improved picture of the XUV absorption across the full photon energy range.

4. CONCLUSIONS

In summary, we have presented an atom-centered basis real-time time-dependent density functional theory (TDDFT) prescription for capturing excitations ranging from low-lying valence to post-ionization (e.g., resonance) states. Here, the "first principles" (ionization potential) tuned range-separated LC-PBE functional in conjunction with a simple phenomenological molecular orbital-based imaginary absorbing potential yields spectra consistent with EELS experiments over the range of 0 to 50 eV for gas-phase C_2H_2 , H_2O , and CF_2Cl_2 , including autoionizing resonance states. The crucial role of the imaginary potential is to "filter out" the spurious virtual states, which should lie in the continuum but are artificially bound as a consequence of the finite basis. This not only removes artifacts from the spectral response, but also purifies high-energy bound excitations which would otherwise include significant contri-

butions from these nonphysical states. By constructing the potential directly in the molecular orbital space, no extra computational cost is incurred, with significant savings over a traditional spatial absorbing boundary, which in a finite basis requires numerous extra "ghost" basis functions to properly function. The main drawback to this approach is that one must carefully pick the form of the absorbing potential, unlike in the spatial potential approach where virtually any smoothly varying potential at the simulation edges will suffice.

Going beyond spectroscopic calculations, this technique is equally applicable to computing photoionization dynamics. In this paper, the simulations were weak-field delta-function simulations which distribute the energy equally over all frequencies, and the overall system charge was not appreciably reduced. In a photoionization dynamics process, on the other hand, an electric field pulse drives electrons from the ground state into a particular excited state, which would then involve significant loss of wave function norm/density matrix trace, and the resulting dynamics could then be monitored in real-time; this will be explored in future studies. Alternately, the imaginary boundary could act as an electron "source" simply by switching the sign in eq 8, which would emulate electrons entering the system through a particular virtual orbital.

AUTHOR INFORMATION

Corresponding Author

*E-mail: klopata@lsu.edu (K.L.), niri.govind@pnnl.gov (N.G.).

Present Address

[†]Department of Chemistry, Louisiana State University, Baton Rouge, LA 70803, USA.

Notes

The authors declare no competing financial interest.

ACKNOWLEDGMENTS

The research was performed at the Environmental Molecular Sciences Laboratory (EMSL), a national scientific user facility sponsored by the U.S. Department of Energy's Office of Biological and Environmental Research and located at the Pacific Northwest National Laboratory (PNNL). PNNL is operated for the Department of Energy by the Battelle Memorial Institute, under Contract DE-AC06-76RLO-1830. K.L. acknowledges the William Wiley Postdoctoral Fellowship from EMSL. N.G. acknowledges support from the U.S. Department of Energy, Office of Basic Energy Sciences, under Grant No. DESC0008666 of the SciDAC program.

REFERENCES

- (1) Schultze, M.; Wirth, A.; Grguras, I.; Uiberacker, M.; Uphues, T.; Verhoef, A.; Gagnon, J.; Hofstetter, M.; Kleineberg, U.; Goulielmakis, E.; Krausz, F. *J. Electron. Spectrosc.* **2011**, *184*, 68–77.
- (2) Strasser, D.; Haber, L. H.; Doughty, B.; Leone, S. R. *Mol. Phys.* **2008**, *106*, 275–280.
- (3) Chen, X.; Larsen, D. S.; Bradforth, S. E.; van Stokkum, I. H. M. *J. Phys. Chem. A* **2011**, *115*, 3807–3819.
- (4) Timmers, H.; Shivaram, N.; Sandhu, A. *Phys. Rev. Lett.* **2012**, *109*, 173001.
- (5) Simons, J. In *Resonances in Electron–Molecule Scattering, Van der Waals Complexes, and Reactive Chemical Dynamics*; Truhlar, D. G., Ed.; American Chemical Society: Washington, D.C., 1984; Chapter 2, pp 3–16.
- (6) Neuhauser, D. *J. Chem. Phys.* **1991**, *95*, 4927–4932.
- (7) Kulander, K. C. *Phys. Rev. A* **1987**, *36*, 2726–2738.
- (8) Harumiya, K.; Kawata, I.; Kono, H.; Fujimura, Y. *J. Chem. Phys.* **2000**, *113*, 8953–8960.

- (9) Mundt, M. J. *Theor. Comput. Chem.* **2009**, 08, 561–574.
- (10) Krueger, A. J.; Maitra, N. T. *Phys. Chem. Chem. Phys.* **2009**, 11, 4655–4663.
- (11) Fronzoni, G.; Stener, M.; Decleva, P. *Chem. Phys.* **2004**, 298, 141–153.
- (12) Reinhardt, W. P. *Annu. Rev. Phys. Chem.* **1982**, 33, 223–255.
- (13) Moiseyev, N. *Phys. Rep.* **1998**, 302, 212–293.
- (14) Kosloff, R.; Kosloff, D. J. *Comput. Phys.* **1986**, 63, 363–376.
- (15) Scrinzi, A. *Phys. Rev. A* **2010**, 81, 053845.
- (16) Telnov, D. A.; Sosnova, K. E.; Rozenbaum, E.; Chu, S.-I. *Phys. Rev. A* **2013**, 87, 053406.
- (17) Yasuike, T.; Yabushita, S. *Chem. Phys. Lett.* **2000**, 316, 257–265.
- (18) Bravaya, K. B.; Zuev, D.; Epifanovsky, E.; Krylov, A. I. *J. Chem. Phys.* **2013**, 138, 124106.
- (19) Seideman, T.; Miller, W. H. *J. Chem. Phys.* **1992**, 96, 4412–4422.
- (20) Baer, R.; Seideman, T.; Ilani, S.; Neuhauser, D. *J. Chem. Phys.* **2004**, 120, 3387–3396.
- (21) Neuhauser, D.; Lopata, K. J. *Chem. Phys.* **2007**, 127, 154715–154715.
- (22) Santra, R.; Cederbaum, L. S. *J. Chem. Phys.* **2001**, 115, 6853–6861.
- (23) Zhou, Y.; Ernzerhof, M. J. *Phys. Chem. Lett.* **2012**, 3, 1916–1920.
- (24) Baer, R.; Kurzweil, Y.; Cederbaum, L. S. *Isr. J. Chem.* **2005**, 45, 161–170.
- (25) Nakatsukasa, T.; Yabana, K. *J. Chem. Phys.* **2001**, 114, 2550–2561.
- (26) Runge, E.; Gross, E. K. U. *Phys. Rev. Lett.* **1984**, 52, 997–1000.
- (27) Marques, M. A.; Maitra, N. T.; Nogueira, F. M.; Gross, E. K.; Rubio, A. *Fundamentals of Time-Dependent Density Functional Theory*; Springer: Berlin, 2012.
- (28) Lopata, K.; Van Kuiken, B. E.; Khalil, M.; Govind, N. *J. Chem. Theory Comput.* **2012**, 8, 3284–3292.
- (29) Van Kuiken, B. E.; Valiev, M.; Daifuku, S. L.; Bannan, C.; Strader, M. L.; Cho, H.; Huse, N.; Schoenlein, R. W.; Govind, N.; Khalil, M. J. *Phys. Chem. A* **2013**, 117, 4444–4454.
- (30) Yabana, K.; Bertsch, G. F. *Phys. Rev. B* **1996**, 54, 4484–4487.
- (31) Jakowski, J.; Morokuma, K. *J. Chem. Phys.* **2009**, 130, 224106.
- (32) Meng, S.; Kaxiras, E. J. *Chem. Phys.* **2008**, 129, 054110.
- (33) Li, X.; Tully, J. C. *Chem. Phys. Lett.* **2007**, 439, 199–203.
- (34) Li, X.; Tully, J. C.; Schlegel, H. B.; Frisch, M. J. *J. Chem. Phys.* **2005**, 123, 084106.
- (35) Lopata, K.; Govind, N. *J. Chem. Theory Comput.* **2011**, 7, 1344–1355.
- (36) van Leeuwen, R.; Baerends, E. J. *Phys. Rev. A* **1994**, 49, 2421–2431.
- (37) Tozer, D. J.; Handy, N. C. *J. Chem. Phys.* **1998**, 109, 10180–10189.
- (38) Casida, M. E.; Salahub, D. R. *J. Chem. Phys.* **2000**, 113, 8918–8935.
- (39) Gaiduk, A. P.; Staroverov, V. N. *J. Chem. Phys.* **2012**, 136, 064116.
- (40) Baer, R.; Livshits, E.; Salzner, U. *Annu. Rev. Phys. Chem.* **2010**, 61, 85–109.
- (41) Srebro, M.; Autschbach, J. J. *Chem. Theory Comput.* **2011**, 8, 245–256.
- (42) Refaely-Abramson, S.; Sharifzadeh, S.; Govind, N.; Autschbach, J.; Neaton, J. B.; Baer, R.; Kronik, L. *Phys. Rev. Lett.* **2012**, 109, 226405.
- (43) Kronik, L.; Stein, T.; Refaely-Abramson, S.; Baer, R. *J. Chem. Theory Comput.* **2012**, 8, 1515–1531.
- (44) Klinkusch, S.; Saalfrank, P.; Klamroth, T. *J. Chem. Phys.* **2009**, 131, 114304.
- (45) Castro, A.; Marques, M. A. L.; Rubio, A. *J. Chem. Phys.* **2004**, 121, 3425–3433.
- (46) Valiev, M.; Bylaska, E. J.; Govind, N.; Kowalski, K.; Straatsma, T. P.; Van Dam, H. J. J.; Wang, D.; Nieplocha, J.; Aprà, E.; Windus, T. L.; de Jong, W. A. *Comput. Phys. Commun.* **2010**, 181, 1477–1489.
- (47) NWChem. <http://www.nwchem-sw.org> (accessed March 2013).
- (48) Feller, D. *J. Comput. Chem.* **1996**, 17, 1571–1586.
- (49) Schuchardt, K. L.; Didier, B. T.; Elsethagen, T.; Sun, L.; Gurumoorathi, V.; Chase, J.; Li, J.; Windus, T. L. *J. Chem. Inf. Model.* **2007**, 47, 1045–1052.
- (50) EMSL Basis Set Exchange. <https://bse.pnl.gov> (accessed March 2013).
- (51) Lopata, K.; Reslan, R.; Kowalska, M.; Neuhauser, D.; Govind, N.; Kowalski, K. *J. Chem. Theory Comput.* **2011**, 7, 3686–3693.
- (52) Petersilka, M.; Gossmann, U. J.; Gross, E. K. U. *Phys. Rev. Lett.* **1996**, 76, 1212–1215.
- (53) Casida, M. E. In *Recent Advances in Density Functional Methods*, Vol. 1; Chong, D. P., Ed.; World Scientific Publishing: Singapore, 1995; Chapter 5, pp 155–192.
- (54) Casida, M.; Huix-Rotllant, M. *Annu. Rev. Phys. Chem.* **2012**, 63, 287–323.
- (55) Brion, C. E. Database of Absolute Dipole Photoabsorption Oscillator Strengths of Atoms and Small Molecules. Available via the Internet at <http://www.chem.ubc.ca/sites/chem.ubc.ca/files/database.zip> (accessed March 2013).
- (56) Avaldi, L.; Dawber, G.; Hall, R.; King, G.; McConkey, A.; MacDonald, M.; Stefani, G. *J. Electron. Spectrosc.* **1995**, 71, 93–105.
- (57) Cooper, G.; Burton, G. R.; Brion, C. J. *Electron. Spectrosc.* **1995**, 73, 139–148.
- (58) Levine, Z. H.; Soven, P. *Phys. Rev. Lett.* **1983**, 50, 2074–2077.
- (59) Kischlat, W.; Morgner, H. J. *Electron. Spectrosc.* **1985**, 35, 273–288.
- (60) Au, J. W.; Burton, G. R.; Brion, C. E. *Chem. Phys.* **1997**, 221, 151–168.
- (61) Kimura, K.; Katsumata, S.; Achiba, Y.; Yamazaki, T.; Iwata, S. *Handbook of HeI Photoelectron Spectra of Fundamental Organic Compounds*; Japan Scientific Society Press: Tokyo, 1981.
- (62) Page, R. H.; Larkin, R. J.; Shen, Y. R.; Lee, Y. T. *J. Chem. Phys.* **1988**, 88, 2249–2263.
- (63) Chan, W. F.; Cooper, G.; Brion, C. E. *Chem. Phys.* **1993**, 178, 387–400.